

# Sb<sup>IV</sup>, an Unusual Player in 2D Spintronic Devices

Christian Tantardini,\* Maryam Azizi, Tariq Altalhi, Alexander G. Kvashnin, Alessio Filippetti, Carlo Gatti, Boris I. Yakobson, and Xavier Gonze\*



Cite This: ACS Nano 2025, 19, 26562–26571



Read Online

ACCESS |

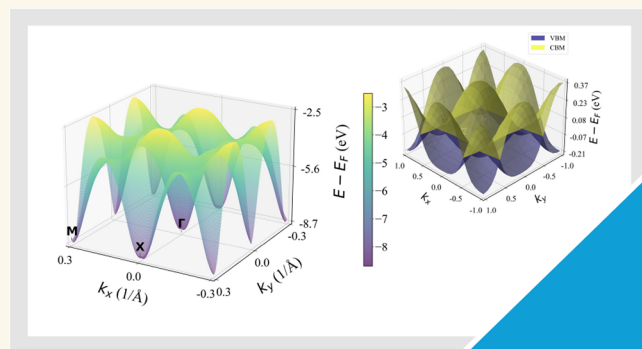
Metrics & More

Article Recommendations

Supporting Information

**ABSTRACT:** We present a first-principles study of ultrathin films of the perovskite Rb<sub>2</sub>SbCl<sub>6</sub>. Density-functional theory calculations combined with Bader charge analysis show that antimony adopts the Sb<sup>4+</sup> oxidation state, and density-functional perturbation theory confirms structural stability for multilayer configurations. The Rb-terminated bilayer displays nodal-line semimetal behavior, characterized by an “egg-shaped” valence- and conduction-band topology that permits sign-reversal doping. The computed Seebeck coefficient is approximately 30  $\mu\text{V K}^{-1}$  at 100 K and trends toward zero at 300 K, while the spin Hall conductivity is about  $10^{-2} \Omega^{-1} \text{cm}^{-1}$ , comparable to values reported for other two-dimensional materials. As the number of layers increases, charge disproportionation arises, with Sb(III) localized at the surface and Sb(V) in inner layers. These results relate structural stability, charge localization, and reduced dimensionality in Rb-terminated Rb<sub>2</sub>SbCl<sub>6</sub> multilayers and indicate inverse-sign thermoelectric and spin Hall responses relevant for spin-charge interconversion in spin-based transistors and nonvolatile memory devices.

**KEYWORDS:** Rb<sub>2</sub>SbCl<sub>6</sub> two-dimensional perovskite, Sb(IV) oxidation state, nodal-line semimetal, inverse Seebeck effect, spin Hall conductivity, spin-charge interconversion



## INTRODUCTION

Antimony (Sb) displays a broad range of oxidation states, from −III to +V. Among these, Sb(III) and Sb(V) are most commonly encountered in both discrete complexes and extended solids.<sup>1–3</sup> By contrast, Sb(IV) is much more elusive. Although Sb(IV) can be generated under carefully controlled conditions in molecular complexes,<sup>4,5</sup> attempts to isolate it in the solid state consistently reveal its thermodynamic propensity to disproportionate into Sb(III) and Sb(V).<sup>6–13</sup> This tendency for Sb(IV) to disproportionate is of considerable interest in materials chemistry and nanoscale design, since mixed-valence antimony phases may exhibit unusual electronic, optical, and magnetic properties.<sup>14,15</sup> Indeed, Mössbauer spectroscopy, celebrated for its sensitivity to local electronic environments, reveals that Sb(IV) rarely persists in extended lattices; instead, it spontaneously disproportionates into Sb(III) and Sb(V).<sup>6–13</sup> Although stability in the form of (Ph<sub>4</sub>Sb<sup>+</sup>) has been documented,<sup>11</sup> Sb(IV) generally remains thermodynamically disfavored in the solid state. Where Sb(IV) does occur, it is frequently stabilized by bulky substituents or strongly donating ligands that impede disproportionation. Early work demonstrated its presence in

tetrahalidoantimonate(IV) anions, such as [SbCl<sub>4</sub>]<sup>−</sup> and [SbBr<sub>4</sub>]<sup>−</sup>, where tight ion pairing and crystal packing support the +IV state.<sup>4,5</sup> Later studies found that Sb(IV) could be “locked” in place within mixed-valent antimony halide or coordination polymer frameworks through halide bridges or donor ligands.<sup>14,15</sup> Other investigations revealed that strongly electron-withdrawing trifluoroacetate ligands also help stabilize Sb(IV) in complexes such as Sb(O<sub>2</sub>CCF<sub>3</sub>)<sub>4</sub>.<sup>16</sup> More recently, bulky ligands like N-heterocyclic carbenes (NHCs) or amidinates have been shown to stabilize Sb(IV) by forming strong Sb–C and Sb–N bonds.<sup>17</sup> Collectively, these examples highlight the importance of ligand design and controlled reaction conditions in maintaining Sb(IV) against disproportionation.

Received: March 24, 2025

Revised: July 8, 2025

Accepted: July 9, 2025

Published: July 17, 2025



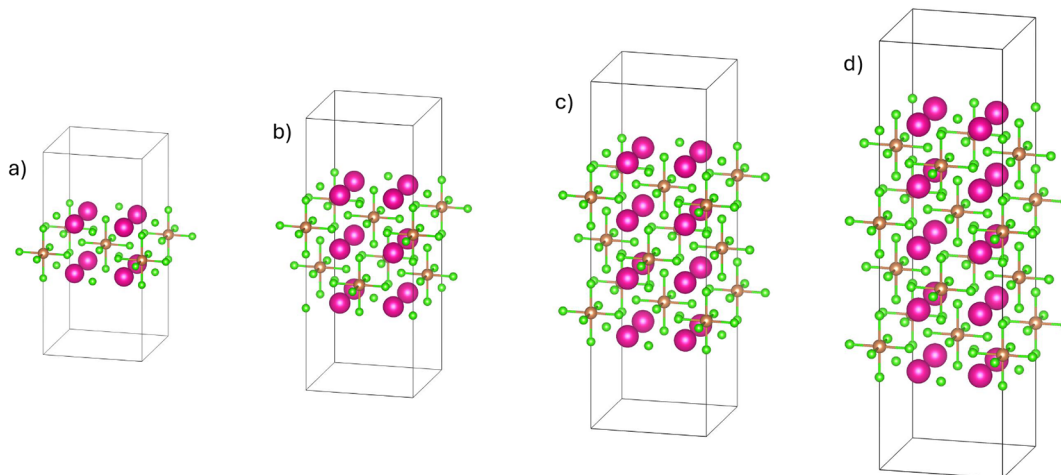


**Figure 1.** Crystal structures of Rb-terminated multilayers derived from the  $\text{Rb}_2\text{SbCl}_6$  conventional cell: (a) bilayer, (b) three-layer, (c) four-layer, and (d) five-layer configurations. Legend: green, chlorine; brown, antimony; purple, rubidium.

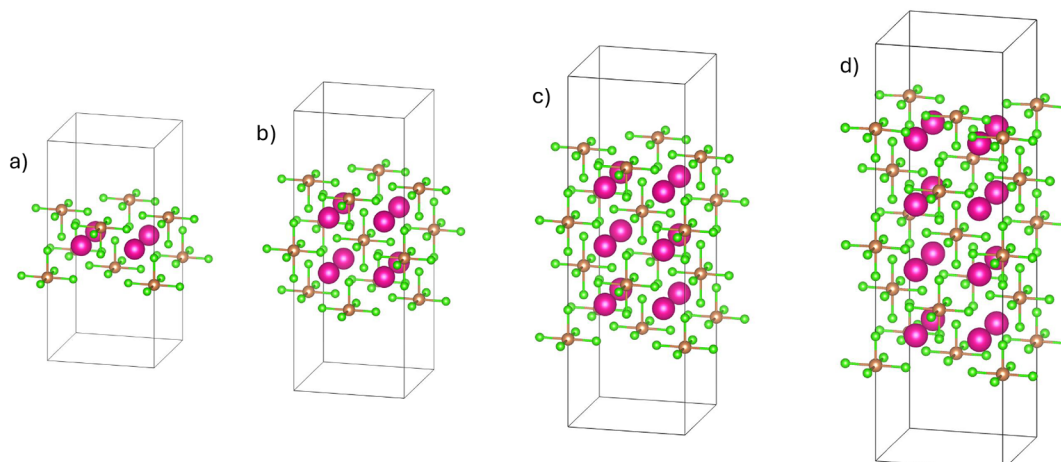


**Figure 2.** Crystal structures of Sb-terminated layers derived from the  $\text{Rb}_2\text{SbCl}_6$  conventional cell: (a) bilayer, (b) three-layer, (c) four-layer, and (d) five-layer configurations. Legend: green, chlorine; brown, antimony; purple, rubidium.

Meanwhile, the pursuit of tunable solid-state properties through doping has fueled interest in substituting antimony for other cations. Sb(III) is especially attractive because its electronic configuration can significantly alter a host lattice's band structure and carrier concentration, thereby improving electronic and optical performance in semiconductors and related materials.<sup>18–27</sup>

Alongside these doping approaches, there is also growing interest in exploiting antimony's unique electronic behavior in two-dimensional materials, particularly for solar cell applications. Indeed, Sb has been incorporated into perovskite-based structures to tailor their optoelectronic properties. An intriguing case is  $\text{Rb}_2\text{SbCl}_6$ , a cubic  $\text{A}_2\text{BX}_6$  belonging to a class of vacancy-ordered double perovskites.<sup>28</sup> In such  $\text{A}_2\text{BX}_6$  materials, half of the B sites in the parent  $\text{ABX}_3$  perovskite framework are systematically removed, resulting in a distinctive arrangement of metal sites. Our study focuses on  $\text{Rb}_2\text{SbCl}_6$ , which the Materials Project (mp-1207160) predicts to be stable based on first-principles calculations. Although this compound has chiefly been explored for its optoelectronic properties,<sup>29</sup> little has been reported regarding its stability under collective displacements.

Interestingly, prior investigations using *Mössbauer spectroscopy* have shown that analogous antimony-based frameworks often undergo disproportionation of Sb(IV) into Sb(III) and Sb(V).<sup>6–13</sup> However, studies of molecular complexes demonstrate that Sb(IV) can be stabilized by halide coordination.<sup>4,5</sup> This insight raises the possibility that 2D antimony materials, which typically feature robust halide coordination environments, might provide a hitherto unexplored platform for both preserving this rare oxidation state and harnessing its unique electronic properties—particularly in the context of next-generation solar cells.

Ultrathin, two-dimensional halide perovskites exhibit remarkable electronic and optical properties, markedly distinct from their bulk counterparts, and offer enhanced stability and tunable bandgaps.<sup>30–32</sup> These low-dimensional architectures also show promise in spintronics—where the intrinsic spin of electrons is harnessed for advanced data storage and processing—enabling faster, more energy-efficient, and higher-density devices.<sup>33–41</sup> Achieving a spin Hall conductivity exceeding  $\sim 10^{-3} \Omega^{-1} \text{ cm}^{-1}$  remains crucial for efficient spin–charge interconversion,<sup>33–41</sup> driving the search for materials with strong spin–orbit coupling (SOC).<sup>42–46</sup> In this context, topological semimetals—including Weyl,<sup>47–51</sup> Dirac,<sup>49–52</sup> and

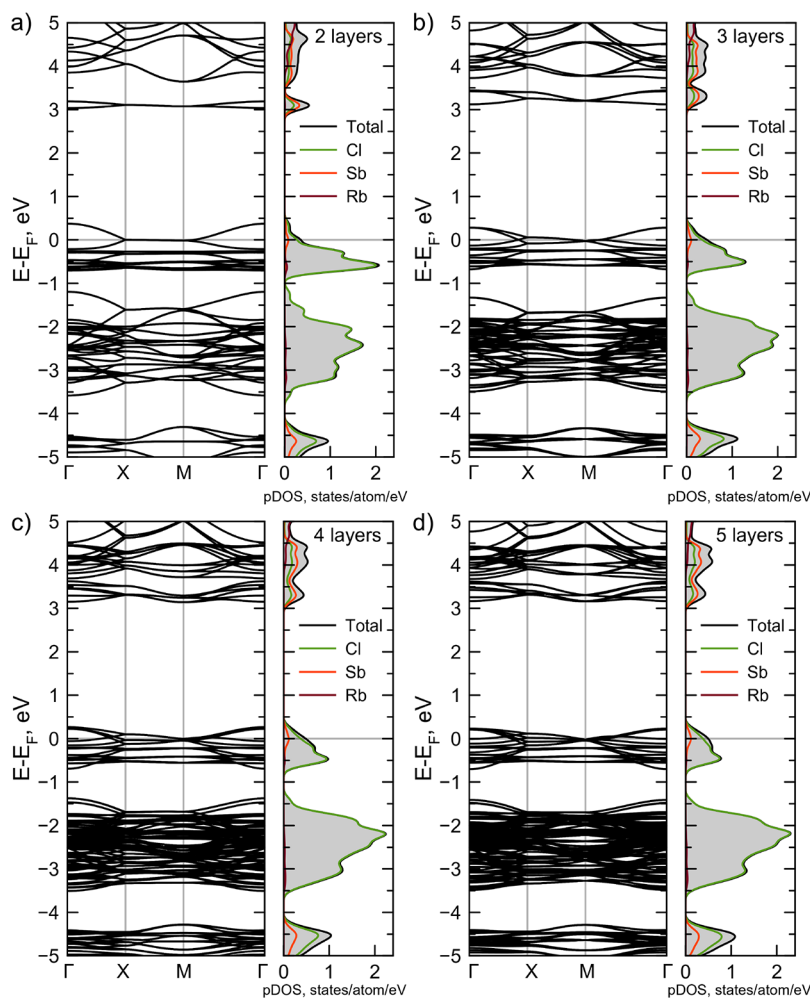


**Figure 3.** KS electronic band structures and projected densities of states (pDOS) for Rb-terminated (a) two-, (b) three-, (c) four-, and (d) five-layer slabs derived from the  $\text{Rb}_2\text{SbCl}_6$  conventional cell, calculated with spin-orbit coupling (SOC) included.

nodal line semimetals<sup>53–56</sup>—have emerged as promising candidates, thanks to their nontrivial band structures and robust SOC that can yield large spin Hall currents.

Here, we investigated the electronic properties of  $\text{Rb}_2\text{SbCl}_6$  multilayers with either Rb- or Sb-terminated surfaces (Figures 1 and 2), focusing on the oxidation state of Sb. Our findings show that the Rb-terminated bilayer exhibits a thermodynamically stable Sb(IV) configuration, featuring an inverted band gap that supports remarkable spin Hall conductivity. These attributes position  $\text{Rb}_2\text{SbCl}_6$  as a compelling ultrathin platform for spintronic applications.

## RESULTS AND DISCUSSION

Below, we describe the Bader charge analysis performed to investigate potential Sb(IV) charge disproportionation in  $\text{Rb}_2\text{SbCl}_6$  multilayers. Bader analysis partitions the electron density into atomic regions bounded by zero-flux surfaces, where the gradient of the electron density is orthogonal to the surface normal.<sup>57–59</sup> This approach offers a quantitative measure of charge distribution, bonding character, and reactivity. Bader charges quantify the net electron count associated with each atom relative to its neutral state,<sup>60–62</sup> and often diverge from formal oxidation states in systems with substantial covalency.<sup>63</sup> Such deviations can be further

explored using topological descriptors<sup>58,63–66</sup> and indices of electron localization/delocalization.<sup>67–71</sup>

In the molecular compounds  $\text{SbCl}_3$  (Sb(III)),  $\text{SbCl}_4$  (Sb(IV)), and  $\text{SbCl}_5$  (Sb(V)), the Bader charges are +1.49, +1.77, and +2.11, respectively. In crystalline  $\text{SbCl}_3$  and  $\text{SbCl}_5$ , the Bader charges are slightly higher, at +1.56 and +2.13, respectively. However, the differences from the molecular values are only 0.07 for Sb(III) and 0.02 for Sb(V), confirming the possibility of comparing the oxidation states of Sb in both molecular compounds and in the bulk. Extending this analysis to the  $\text{Rb}_2\text{SbCl}_6$  multilayers (Tables S2X–S9X) reveals similar behavior between Rb-terminated and Sb-terminated surfaces.

In Rb-terminated multilayers, the bi- and three-layer configurations exhibit antimony atoms with identical Bader charges of +1.77 (Sb(IV)). In Sb-terminated multilayers, those same configurations show +1.65 (also near Sb(IV)). As additional layers are added in both terminations, surface antimony shifts progressively toward Sb(III), while deeper antimony approaches Sb(V). This effect intensifies with increasing thickness, mirroring the Sb(III)/Sb(V) disproportionation found by Mössbauer spectroscopy in bulk samples,<sup>12</sup> although even at five layers the systems have yet to reach the fully bulk-like degree of disproportionation.

These discrepancies align with observed changes in Sb–Cl bond lengths: in Rb-terminated surfaces, axial bonds lengthen

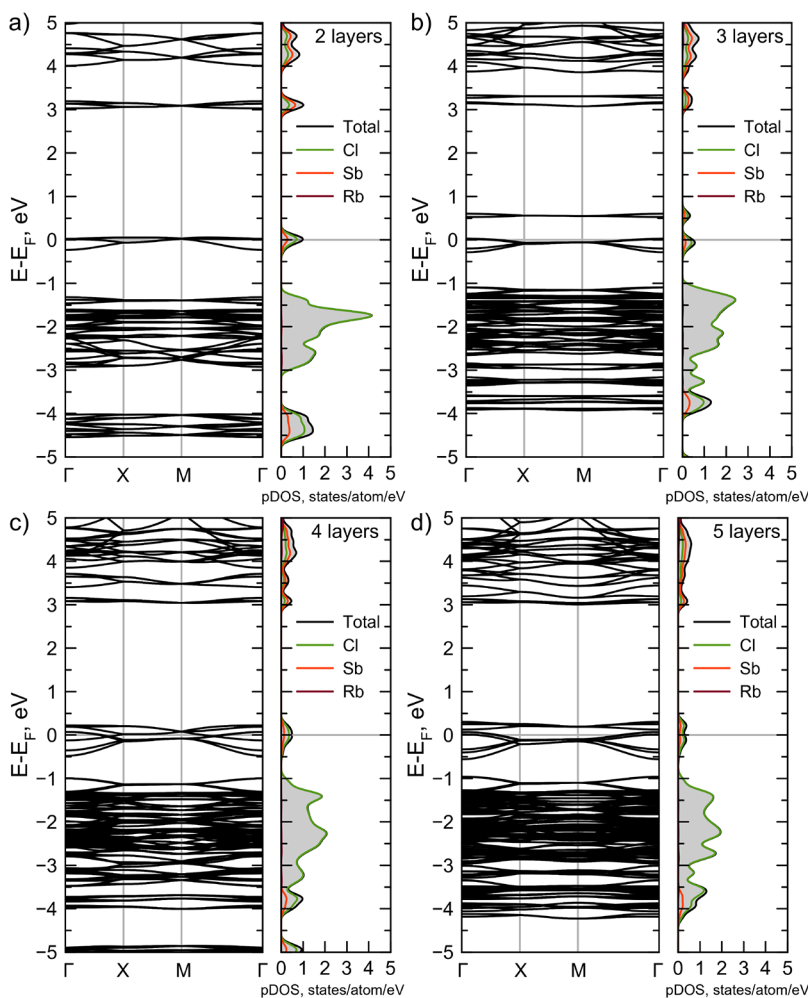


**Figure 4.** KS electronic band structures and projected densities of states (pDOS) for Sb-terminated (a) two-, (b) three-, (c) four-, and (d) five-layer slabs derived from the  $\text{Rb}_2\text{SbCl}_6$  conventional cell, calculated with spin-orbit coupling (SOC) included.

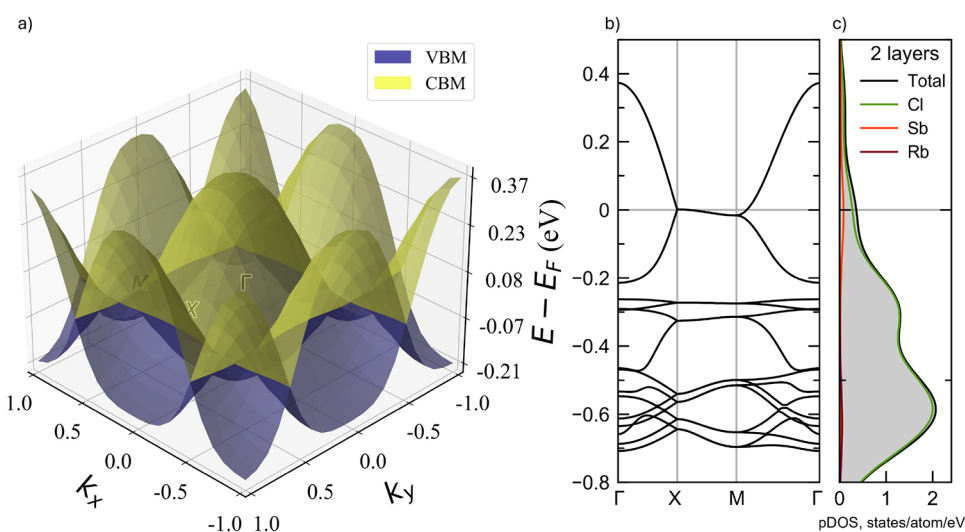


**Figure 5.** For the Rb-terminated bilayer cut from the conventional cell of  $\text{Rb}_2\text{SbCl}_6$ : (a) 3D plot of the valence band maxima (VBM) and conduction band minima (CBM) in the Brillouin zone; (b) 2D plot around the Fermi level of the Kohn-Sham (KS) electronic structure with spin-orbit coupling (SOC); and (c) projected density of states (pDOS).

slightly (around 2.63–2.64 Å), while in Sb-terminated surfaces they can shorten to approximately 2.38–2.46 Å. In both cases, equatorial bond lengths exhibit mixed trends, reflecting the

complex interplay between electron distribution and structural factors at the surface. As the layer count increases, interior bond lengths and charges trend closer to those of the bulk, yet

surface effects persist at the nanoscale. Overall, these results emphasize the significant influence of surface termination and reduced dimensionality on Sb oxidation states and bonding in  $\text{Rb}_2\text{SbCl}_6$ . In Rb-terminated systems, both the bilayer and three-layer configurations retain a predominantly Sb(IV) state, while in Sb-terminated systems, the bilayer likewise shows Sb(IV). However, thicker multilayers increasingly exhibit charge separation between surface and interior Sb atoms, paralleling the Sb(III)/Sb(V) disproportionation observed in bulk samples. This sensitivity to layer thickness and termination underscores the critical importance of controlling surface conditions to preserve Sb(IV) and its associated electronic properties in low-dimensional perovskite frameworks. Bader analysis indicates that antimony atoms adopt a predominantly Sb(IV) state in the thinner multilayers (up to three layers for Rb-terminated, two layers for Sb-terminated), with increasing separation toward Sb(III) and Sb(V) at the surface and interior sites in thicker systems. Despite this nominal Sb(IV) assignment—often associated with a band-filling scenario conducive to semiconducting properties—the Kohn–Sham band structures of these  $\text{Rb}_2\text{SbCl}_6$  multilayers reveal a semimetallic behavior (Figures 3 and 4), with multiple bands crossing the Fermi level. Specifically, an almost flat band appears near the Fermi level, separated by a sizable gap ( $\sim 3$  eV) from the Sb(*p*)-dominated conduction band. This flat band, derived primarily from localized Sb(5s) and Cl(3p) orbitals, underscores how the oxidation states implied by Bader charges do not straightforwardly translate into a simple semiconducting picture in few-layer systems. Instead, the interplay between localized orbitals, layer-dependent charge redistribution, and surface-induced structural relaxation fosters an electronic structure closer to that of a semimetal.

Below, we focus on the particularly noteworthy features of the Rb-terminated bilayer. As shown by the three-dimensional plots of its valence band maximum (VBM) and conduction band minimum (CBM) in Figure 5a, both bands exhibit an inverse parabolic dispersion, with the VBM (CBM) at  $\Gamma$ . Along the Brillouin zone edges ( $X$ – $M$ ), these two bands come into contact (Figure 5b), producing an “egg-shaped” band configuration reminiscent of a nodal line semimetal and allowing for inverse sign doping.

Such “inverse sign doping” mirrors behavior observed in advanced materials with intricate band inversions, including topological insulators<sup>72–75</sup> and Weyl semimetals.<sup>76–79</sup> In our bilayer, two high-symmetry points in the Brillouin zone ( $X$  and  $M$ ) exhibit degeneracies that could, at first glance, be indicative of Weyl nodes. To investigate this possibility, we constructed a tight-binding Hamiltonian and performed Wannier Charge Center (WCC) calculations<sup>80</sup> using Z2PACK, guided by prior theoretical predictions.<sup>81</sup> Our results confirmed that both degeneracies are characterized by zero chirality, implying that nonsymmorphic symmetry operations—rather than topological Weyl physics—are responsible for these band crossings.

Despite ruling out Weyl nodes, this band structure still portends interesting transport phenomena. Next, an examination of the Fermi surface near the Fermi level (Figure 6a–c) reveals partially flattened pockets, a hallmark of unconventional electronic transport. Consequently, the Seebeck coefficient  $S$  (Figure 6d,e) exhibits a crossover from positive to negative values at higher temperatures, reflecting an interplay between thermal excitations and doping-induced band filling, which is inverse Seebeck coefficient.<sup>82–84</sup>

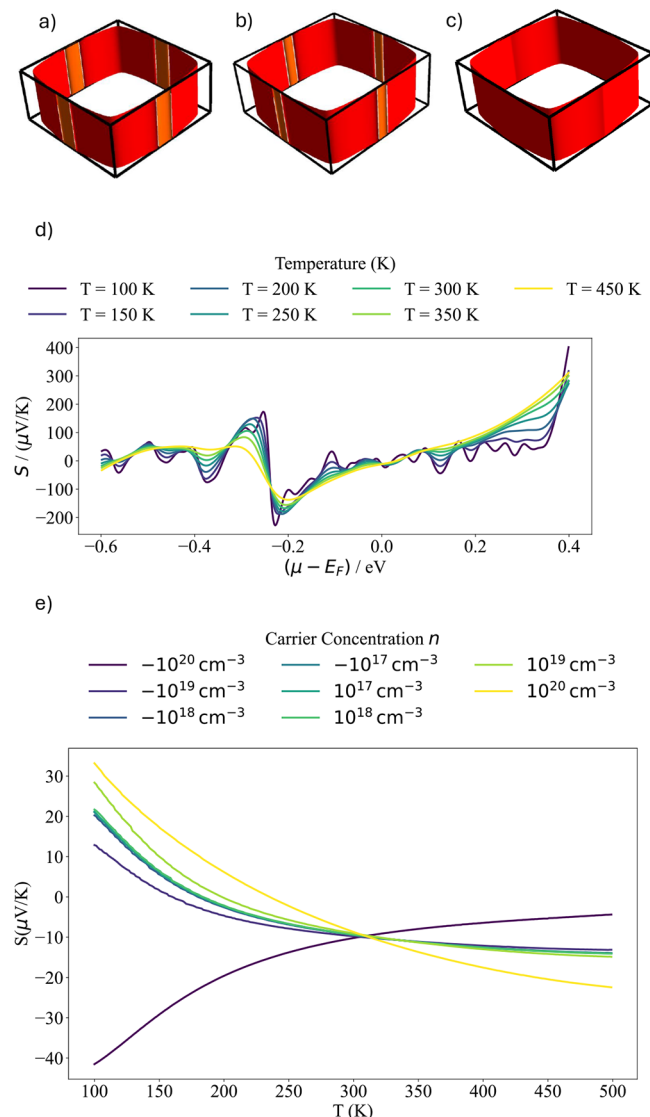


**Figure 6.** Plot of Fermi surface within the Brillouin zone at Fermi level (a) 0.0005 eV, (b) 0.001 eV and (c) 0.1 eV. The valence band maxima (VBM), orange, and conduction band minima (CBM), red. (d) Seebeck coefficient as a function of chemical potential  $\mu$  scaled by Fermi energy  $E_F$  for different Temperatures. (e) Seebeck coefficient as a function of Temperature for different concentration of hole and electrons.

An inverted sign in Seebeck means that, for a given temperature gradient, the build-up potential at the two sides of the bar will have opposite verse with respect to the normal behavior; this is especially interesting in field-effect thermoelectric applications since in our bilayer the Fermi energy falls right at the basal plane of the two half-domes, thus a tiny charge depletion/replenishment can switch the sign of the accumulated build-up. The same occurs for the spin-Hall effect: the reverted sign means that the spin voltage accumulated at the edges of the bilayer has a reversed sign compared to the usual behavior.

Finally, we analyzed the spin-dependent transport by computing the spin Hall Berry curvature (Figure 7) and the resulting spin Hall conductivity (SHC), Figure 8. We obtained an SHC of approximately  $10^{-2} \Omega^{-1} \text{cm}^{-1}$  near the Fermi energy, comparable to that of other promising two-dimensional (2D) spintronic materials.<sup>85–89</sup> Together, these findings

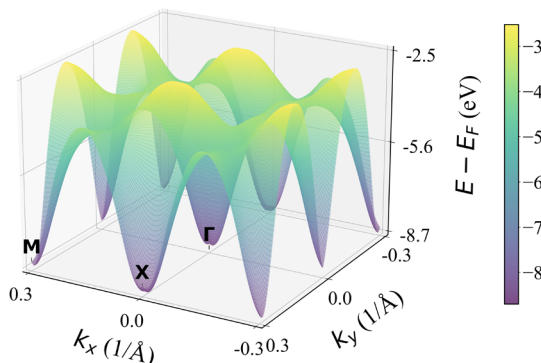


**Figure 7.** Spin Hall Berry curvature within the reciprocal space.

underscore the strong potential of the Rb-terminated bilayer for advanced electronic and spintronic applications, leveraging its distinctive band structure, robust spin-orbit coupling, and proven structural stability.

Our comprehensive study reveals that the Rb-terminated bilayer of  $\text{Rb}_2\text{SbCl}_6$  is not only electronically intriguing—with its predominantly Sb(IV) oxidation state and semimetallic band structure—but also structurally robust. First-principles

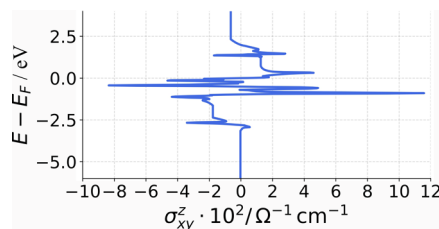


**Figure 8.** Spin Hall conductivity computed from the spin Hall Berry curvature.

phonon calculations (Figure 9) show no imaginary frequencies, confirming its dynamic stability. Furthermore, we performed Born–Oppenheimer molecular dynamics (BOMD) simulation at 300 K to investigate whether such a structure could, in

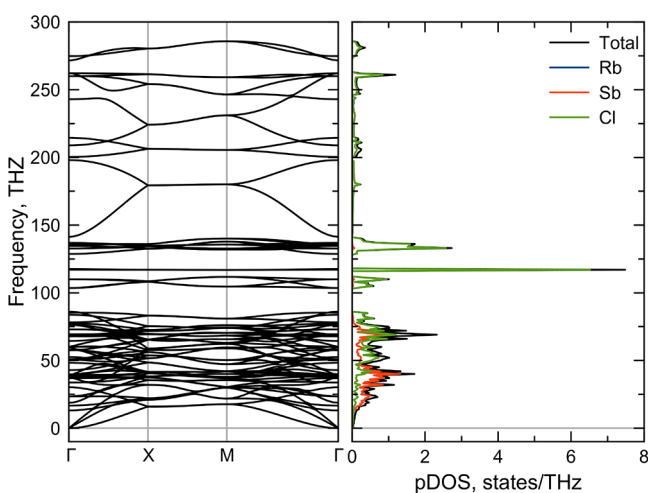


**Figure 9.** Phonon band structure calculated using a  $2 \times 2 \times 1$   $q$ -points mesh for the Rb-terminated bilayer cut from the  $\text{Rb}_2\text{SbCl}_6$  conventional cell. The figure includes Born–Huang invariance conditions and the phonon density of states projected onto different atomic types.

principle, be synthesized at room temperature. From the outset we selected the Rb-terminated bilayer, which contains two symmetry-nonequivalent Sb atoms, because it might undergo Sb(III)/Sb(V) disproportionation; however, no such disproportionation was observed. We therefore carried out BOMD on the same structure to evaluate its dynamical stability. We observed that after approximately 0.15 ps, both the potential energy and the RMSD settle into a clear plateau: the potential energy fluctuates by only 0.280 eV, see in Supporting Information Figure S1, indicating that bond lengths, angles, and electronic contributions remain confined to small, thermally driven variations within a single energy basin rather than exploring new minima. Simultaneously, see in Supporting Information Figure S2, the structural deviation varies by only 0.020 Å—well below typical thresholds for genuine conformational rearrangement—confirming that the atoms oscillate around their equilibrium positions without significant drift. To verify that the system had not migrated into a different minimum during this perturbation phase, the final geometry at the end of the plateau was extracted and subjected to a static relaxation at 0 K; this optimization returned exactly to the same 0 K structure from which the dynamics had begun, demonstrating that the trajectory remains confined to the original equilibrium basin throughout the simulation. Taken together, the narrow energy fluctuations, the negligible structural drift, and the 0 K relaxation confirm that the molecular assembly has reached a state of true dynamic equilibrium, sampling a stable region of phase space characterized by thermal vibrations around a single reference geometry. This combination of unique electronic properties and confirmed stability underlines the potential of the Rb-terminated bilayer for device applications, particularly in ultrathin perovskite-based electronic and optoelectronic architectures.

## CONCLUSIONS

In this study, we conducted a comprehensive first-principles investigation of the electronic and structural properties of multilayer forms of  $\text{Rb}_2\text{SbCl}_6$ . Bader charge analysis integrated with density functional theory (DFT) calculations revealed that antimony adopts the rare Sb(IV) oxidation state in both Rb-terminated and Sb-terminated ultrathin layers. In particular, the Rb-terminated bilayer was found to be thermodynamically stable, as confirmed by density functional perturbation theory (DFPT) calculations showing no imaginary phonon frequencies. However, as the number of layers increases, disproportionation occurs, with Sb(III) localized at the surface and Sb(V) in the inner layers—underscoring the sensitivity of the oxidation state to the multilayer environment.

Transport calculations for the Rb-terminated bilayer indicate an inverse sign Seebeck coefficient of approximately  $30 \mu\text{V/K}$  at 100 K, which diminishes toward zero near 300 K. Additionally, the bilayer exhibits an inverse sign spin Hall conductivity on the order of  $10^{-2} \Omega^{-1} \text{cm}^{-1}$ , comparable to established two-dimensional spintronic materials. These effects underscore the bilayer's efficiency in spin-charge interconversion processes.

In summary, the Rb-terminated bilayer of  $\text{Rb}_2\text{SbCl}_6$  emerges as a promising candidate for next-generation spintronic architectures and innovative electronic applications. Its substantial spin Hall conductivity and unique inverse Seebeck behavior, combined with the stable Sb(IV) oxidation state and favorable electronic band structure, position it at the forefront

of materials suitable for advanced spin-based transistors and nonvolatile memory technologies. Overall, our results elucidate the intricate interplay of structural stability, electron localization, and reduced dimensionality in multilayer  $\text{Rb}_2\text{SbCl}_6$ , and identify its inverse sign thermoelectric and spin Hall properties as key drivers for future electronic and spintronic innovations.

## COMPUTATIONAL DETAILS

All ab initio calculations were performed using the Quantum ESPRESSO (QE) package (version 7.3).<sup>90,91</sup> The Perdew–Burke–Ernzerhof (PBE) exchange-correlation (XC) functional<sup>92</sup> was employed in conjunction with optimized norm-conserving Vanderbilt pseudopotentials (ONCVPs)<sup>93</sup> obtained from the PseudoDojo database<sup>94,95</sup> (<http://www.pseudo-dojo.org>). Spin–orbit coupling (SOC) was included in all calculations.

The electronic wave functions were expanded in a plane-wave (PW) basis with a kinetic energy cutoff of 120 Ry. Brillouin zone integrations were performed using Monkhorst–Pack (MP)  $k$ -point grids, and a Gaussian smearing of 0.010 Ry was applied to improve convergence.<sup>96</sup> Self-consistent field (SCF) calculations were deemed converged when the total energy difference between iterations was less than  $10^{-8}$  Ry.

Starting from the conventional cell of  $\text{Fm}\bar{3}\text{m}-\text{Rb}_2\text{SbCl}_6$  (36 atoms) Rb- or Sb-terminated multilayers were constructed with thicknesses from 2 to 5 layers (Figures 1 and 2). For these two-dimensional structures, a  $10 \times 10 \times 1$   $k$ -point mesh was employed, and an 8 Å vacuum gap along the  $c$ -axis was introduced to minimize spurious periodic interactions.

Geometry optimizations were carried out using the Broyden–Fletcher–Goldfarb–Shanno (BFGS) algorithm.<sup>97–100</sup> Convergence criteria required that the maximum force on each atom be lower than  $5 \times 10^{-8}$  Ry/Å.

Fermi surface analyses were performed using PAOFLOW2.0,<sup>101</sup> employing a  $50 \times 50 \times 50$   $k$ -point mesh. The FermiSurfer code<sup>102</sup> was used for visualization, enabling the identification of features such as electron and hole pockets, Fermi surface nesting, and anisotropies in the electronic structure.

Bader charge analysis was conducted with CRITIC2<sup>103,104</sup> using all-electron densities computed by FHI-aims,<sup>105,106</sup> based on the geometries optimized in Quantum ESPRESSO with same used SCF convergence criteria. This approach partitions the electron density among atoms via electron density gradient zero-flux surfaces, providing insight into charge distribution.

Phonon calculation for the Rb-terminated bilayer was performed using density functional perturbation theory (DFPT) with  $2 \times 2 \times 1$   $q$ -vector grid. The Born–Huang conditions<sup>107</sup> were used to recover the quadratic dispersions of flexural phonons in low-dimensional materials. Convergence was ensured by reducing the potential residual below  $10^{-18}$  Ry.

Born–Oppenheimer molecular dynamics simulations was carried out at 300 K on the Rb-terminated bilayer of the conventional cell of  $\text{Fm}\bar{3}\text{m}-\text{Rb}_2\text{SbCl}_6$ , see Figure 1a with 26 atoms. The time step was set to 20.67 au (1 fs), and a total of 1000 steps (1 ps) were propagated using the Verlet integrator with simple velocity rescaling every 100 steps ( $\sim 100$  fs) to maintain the temperature at 300 K. A  $4 \times 4 \times 1$  Monkhorst–Pack  $k$ -point grid (with no symmetry reduction) was used for Brillouin-zone sampling.

Weyl points were searched using PAOFLOW2.0 through a systematic analysis of band crossings in reciprocal space. The

chirality (topological charge) of each Weyl point was evaluated using Z2PACK.<sup>108</sup>

Finally, the spin Hall conductivity was computed from the spin Berry curvature, also using PAOFLOW2.0. While, the Seebeck coefficient was determined with BoltzTraP2<sup>109</sup> by applying a smoothed Fourier interpolation of the electronic bands.

## ASSOCIATED CONTENT

### SI Supporting Information

The Supporting Information is available free of charge at <https://pubs.acs.org/doi/10.1021/acsnano.5c05027>.

Tables containing the atomic coordinates of all optimized molecular and crystal structures, together with their corresponding Bader atomic charges (PDF)

## AUTHOR INFORMATION

### Corresponding Authors

Christian Tantardini – Center for Integrative Petroleum Research, King Fahd University of Petroleum and Minerals, Dhahran 31261, Saudi Arabia;  [orcid.org/0000-0002-2412-9859](https://orcid.org/0000-0002-2412-9859); Email: [christiantantardini@ymail.com](mailto:christiantantardini@ymail.com)

Xavier Gonze – Université Catholique de Louvain, Louvain-la-Neuve B-1348, Belgium;  [orcid.org/0000-0002-8377-6829](https://orcid.org/0000-0002-8377-6829); Email: [xavier.gonze@uclouvain.be](mailto:xavier.gonze@uclouvain.be)

### Authors

Maryam Azizi – Université Catholique de Louvain, Louvain-la-Neuve B-1348, Belgium

Tariq Altalhi – Chemistry Department, Taif University, Taif 26571, Saudi Arabia

Alexander G. Kvashnin – National University of Science and Technology MISiS, Moscow 119049, Russian Federation

Alessio Filippetti – Dipartimento di Fisica, Università degli Studi di Cagliari, Cittadella Universitaria Monserrato, Cagliari 09042, Italy; CNR-Istituto Officina dei Materiali (IOM), Cagliari, Cittadella Universitaria, Monserrato, CA 09042, Italy;  [orcid.org/0000-0002-9144-7005](https://orcid.org/0000-0002-9144-7005)

Carlo Gatti – CNR - Consiglio Nazionale delle Ricerche, SCITEC - Istituto di Scienze e Tecnologie Chimiche "Giulio Natta", Milan 20133, Italy;  [orcid.org/0000-0002-0047-1596](https://orcid.org/0000-0002-0047-1596)

Boris I. Yakobson – Department of Materials Science and NanoEngineering, Rice University, Houston, Texas 77005, United States; Chemistry Department, Taif University, Taif 26571, Saudi Arabia;  [orcid.org/0000-0001-8369-3567](https://orcid.org/0000-0001-8369-3567)

Complete contact information is available at:

<https://pubs.acs.org/10.1021/acsnano.5c05027>

### Notes

The authors declare no competing financial interest.

## ACKNOWLEDGMENTS

The authors would like to thank Dr. Davide Ceresoli from CNR for his assistance with PAOFLOW and BOMD. A.F. acknowledges project PRIN 2022 “TOTEM”, grant no. FS3D23001080006, funded by the Italian Ministry of University and Research (MUR) and project PNRR-PRIN 2022 “MAGIC”, grant no. FS3D23008340001, funded by the EU. This work was supported by the Fonds de la Recherche Scientifique (FRS-FNRS Belgium) through the PdR Grant No. T.0103.19 – ALPS. It is an outcome of the Shapeable 2D

magnetoelectronics by design project (SHAPEme, EOS Project No. 560400077525) that has received funding from the FWO and FRS-FNRS under the Belgian Excellence of Science (EOS) program. T.A. and B.I.Y. acknowledge the Taif University Research Support Project TURSPHC2025-26/1, Saudi Arabia.

## REFERENCES

- (1) Filella, M.; Williams, P. A.; Belzile, N. Antimony in the environment: knowns and unknowns. *Environmental Chemistry* **2009**, *6*, 95–105.
- (2) Frezard, F.; Demicheli, C.; Kato, K. C.; Reis, P. G.; Lizarazo-Jaimes, E. H. Chemistry of antimony-based drugs in biological systems and studies of their mechanism of action. *Reviews in Inorganic Chemistry* **2013**, *33*, 1–12.
- (3) Multani, R. S.; Feldmann, T.; Demopoulos, G. P. Antimony in the metallurgical industry: A review of its chemistry and environmental stabilization options. *Hydrometallurgy* **2016**, *164*, 141–153.
- (4) Shinohara, N.; Ohshima, M. Production of Sb(IV) Chloro Complex by Flash Photolysis of the Corresponding Sb(III) and Sb(V) Complexes in CH<sub>3</sub>CN and CHCl<sub>3</sub>. *Bull. Chem. Soc. Jpn.* **2000**, *73*, 1599–1604.
- (5) Jiang, J.; Materna, K. L.; Hedström, S.; Yang, K. R.; Crabtree, R. H.; Batista, V. S.; Brudvig, G. W. Antimony Complexes for Electrocatalysis: Activity of a Main-Group Element in Proton Reduction. *Angew. Chem., Int. Ed.* **2017**, *56*, 9111–9115.
- (6) Brukhanov, V.; Iofa, B.; Kotkhekar, V.; Semenov, S.; Shpinel', V. Isomer Chemical Shifts of the Mössbauer Gamma Line in Isoelectronic Antimony Compounds. *Soviet JEP* **1968**, *26*, 912.
- (7) Gukasyan, S.; Shpinel, V. Mössbauer Effect in Antimony-Organic Compounds. *physica status solidi (b)* **1968**, *29*, 49–52.
- (8) Long, G.; Stevens, J.; Bowen, L.; Ruby, S. The oxidation number of antimony in antimony pentasulfide. *Inorganic and Nuclear Chemistry Letters* **1969**, *5*, 21–25.
- (9) Long, G.; Stevens, J.; Bowen, L. 121Sb Mössbauer spectra of antimony oxides. *Inorganic and Nuclear Chemistry Letters* **1969**, *5*, 799–804.
- (10) Bowen, L.; Stevens, J. G.; Long, G. G. *J. Chem. Phys.* **1969**, *51*, 2010.
- (11) Long, G.; Stevens, J.; Tullbane u, R. J.; Bowen, L. H. *J. Am. Chem. Soc.* **1970**, *92*, 4230.
- (12) Birchall, T.; Della Valle, B.; Martineau, E.; Milne, J. Antimony-121 Mössbauer spectroscopy of some chloro-complexes of antimony. *J. Chem. Soc., A: Inorg., Phys., Theor.* **1971**, 1855–1857.
- (13) Della Valle, B. P. A Mössbauer Spectroscopic Investigation of Inorganic Antimony Compounds, M.Sc. Thesis; McMaster University: Hamilton, Ontario, Canada, 1971.
- (14) Adonin, S. A.; Bondarenko, M. A.; Abramov, P. A.; Novikov, A. S.; Plyusnin, P. E.; Sokolov, M. N.; Fedin, V. P. Bromo- and Polybromoantimonates(V): Structural and Theoretical Studies of Hybrid Halogen-Rich Halometalate Frameworks. *Chem. – Eur. J.* **2018**, *24*, 10165–10170.
- (15) Adonin, S. A.; Udalova, L. I.; Abramov, P. A.; Novikov, A. S.; Yushina, I. V.; Korolkov, I. V.; Semitut, E. Y.; Derzhavskaya, T. A.; Stevenson, K. J.; Troshin, P. A.; Sokolov, M. N.; Fedin, V. P. A Novel Family of Polyiodo-Bromoantimonate(III) Complexes: Cation-Driven Self-Assembly of Photoconductive Metal-Polyhalide Frameworks. *Chem. – Eur. J.* **2018**, *24*, 14707–14711.
- (16) Ferguson, G.; Kaitner, B.; Glidewell, C.; Smith, S. High metal coordination numbers in group 15 organometallics: crystal structures of triphenylbismuthbis(trifluoroacetate) and triphenylantimonybis(trifluoroacetate). *J. Organomet. Chem.* **1991**, *419*, 283–291.
- (17) Krüger, J.; Wölper, C.; Auer, A. A.; Schulz, S. Formation and Cleavage of a Sb-Sb Double Bond: From Carbene-Coordinated Distibenes to Stibinidenes. *Eur. J. Inorg. Chem.* **2022**, *2022*, No. e202100960.
- (18) Teller, R. G.; Antonio, M. R.; Brazdil, J. F.; Grasselli, R. K. New materials synthesis: characterization of some metal-doped antimony oxides. *J. Solid State Chem.* **1986**, *64*, 249–260.
- (19) Mishra, K.; Johnson, K.; Schmidt, P. Electronic structure of antimony-doped tin oxide. *Phys. Rev. B* **1995**, *51*, 13972.
- (20) Shanthi, S.; Subramanian, C.; Ramasamy, P. Growth and characterization of antimony doped tin oxide thin films. *J. Cryst. Growth* **1999**, *197*, 858–864.
- (21) Bhattacharya, S.; Pope, A.; Littleton, R., IV; Tritt, T. M.; Ponnambalam, V.; Xia, Y.; Poon, S. Effect of Sb doping on the thermoelectric properties of Ti-based half-Heusler compounds, TiNiSn 1 - x Sb x. *Appl. Phys. Lett.* **2000**, *77*, 2476–2478.
- (22) Santos-Pena, J.; Brousse, T.; Sanchez, L.; Morales, J.; Schleich, D. Antimony doping effect on the electrochemical behavior of SnO<sub>2</sub> thin film electrodes. *J. Power Sources* **2001**, *97*, 232–234.
- (23) Grzeta, B.; Tkalcic, E.; Goebbert, C.; Takeda, M.; Takahashi, M.; Nomura, K.; Jaksic, M. Structural studies of nanocrystalline SnO<sub>2</sub> doped with antimony: XRD and Mossbauer spectroscopy. *J. Phys. Chem. Solids* **2002**, *63*, 765–772.
- (24) Elangovan, E.; Ramamurthi, K. A study on low cost-high conducting fluorine and antimony-doped tin oxide thin films. *Appl. Surf. Sci.* **2005**, *249*, 183–196.
- (25) Babar, A.; Shinde, S.; Moholkar, A.; Bhosale, C.; Kim, J.; Rajpure, K. Physical properties of sprayed antimony doped tin oxide thin films: The role of thickness. *Journal of Semiconductors* **2011**, *32*, No. 053001.
- (26) Jeon, I.-Y.; Choi, M.; Choi, H.-J.; Jung, S.-M.; Kim, M.-J.; Seo, J.-M.; Bae, S.-Y.; Yoo, S.; Kim, G.; Jeong, H. Y.; et al. Antimony-doped graphene nanoplatelets. *Nat. Commun.* **2015**, *6*, 7123.
- (27) Alsmadi, A.; Salameh, B.; Kerr, L. L.; Eid, K. Influence of Antimony doping on the electronic, optical and luminescent properties of ZnO microrods. *Physica B: Condensed Matter* **2018**, *S45*, 519–526.
- (28) Rahim, W.; Cheng, A.; Lyu, C.; Shi, T.; Wang, Z.; Scanlon, D. O.; Palgrave, R. G. Geometric Analysis and Formability of the Cubic A2BX<sub>6</sub> Vacancy-Ordered Double Perovskite Structure. *Chem. Mater.* **2020**, *32*, 9573–9583.
- (29) Berri, S.; Bouarissa, N. First-principles calculations on novel Rb-based halide double perovskites alloys for spintronics and optoelectronic applications. *Optics and Photonics Journal* **2024**, *14*, 1–22.
- (30) Chen, M.; Ju, M.-G.; Garces, H. F.; Carl, A. D.; Ono, L. K.; Hawash, Z.; Zhang, Y.; Shen, T.; Qi, Y.; Grimm, R. L.; et al. Highly stable and efficient all-inorganic lead-free perovskite solar cells with native-oxide passivation. *Nat. Commun.* **2019**, *10*, 16.
- (31) Zhang, Z.; Sun, Q.; Lu, Y.; Lu, F.; Mu, X.; Wei, S.-H.; Sui, M. Hydrogenated Cs<sub>2</sub>AgBiBr<sub>6</sub> for significantly improved efficiency of lead-free inorganic double perovskite solar cell. *Nat. Commun.* **2022**, *13*, 3397.
- (32) Zhang, Y.; Liu, Y.; Xu, Z.; Ye, H.; Yang, Z.; You, J.; Liu, M.; He, Y.; Kanatzidis, M. G.; Liu, S. Nucleation-controlled growth of superior lead-free perovskite Cs<sub>3</sub>Bi<sub>2</sub>I<sub>9</sub> single-crystals for high-performance X-ray detection. *Nat. Commun.* **2020**, *11*, 2304.
- (33) Ahn, E. C. 2D materials for spintronic devices. *npj 2D Mater. Appl.* **2020**, *4*, 17.
- (34) Hirohata, A.; Takanashi, K. Future perspectives for spintronic devices. *J. Phys. D: Appl. Phys.* **2014**, *47*, 193001.
- (35) Guo, L.; Gu, X.; Zhu, X.; Sun, X. Recent advances in molecular spintronics: Multifunctional spintronic devices. *Adv. Mater.* **2019**, *31*, No. 1805355.
- (36) Guo, L.; Hu, S.; Gu, X.; Zhang, R.; Wang, K.; Yan, W.; Sun, X. Emerging spintronic materials and functionalities. *Adv. Mater.* **2024**, *36*, No. 2301854.
- (37) Long, G.; Sabatini, R.; Saidaminov, M. I.; Lakhwani, G.; Rasmita, A.; Liu, X.; Sargent, E. H.; Gao, W. Chiral-perovskite optoelectronics. *Nature Reviews Materials* **2020**, *5*, 423–439.
- (38) Trier, F.; Noël, P.; Kim, J.-V.; Attané, J.-P.; Vila, L.; Bibes, M. Oxide spin-orbitronics: spin–charge interconversion and topological spin textures. *Nature Reviews Materials* **2022**, *7*, 258–274.

- (39) Rimmller, B. H.; Pal, B.; Parkin, S. S. Non-collinear antiferromagnetic spintronics. *Nat. Rev. Mater.* **2024**, *10*, 109–127.
- (40) Guo, Y.; Zhang, X.; Huang, Z.; Chen, J.; Luo, Z.; Zhang, J.; Li, J.; Zhang, Z.; Zhao, J.; Han, X.; et al. Quantum materials for spintronic applications. *npj Spintron.* **2024**, *2*, 36.
- (41) Žutić, I.; Fabian, J.; Sarma, S. D. Spintronics: Fundamentals and applications. *Rev. Mod. Phys.* **2004**, *76*, 323.
- (42) Nandy, S.; Taraphder, A.; Tewari, S. Berry phase theory of planar Hall effect in topological insulators. *Sci. Rep.* **2018**, *8*, 14983.
- (43) Novoselov, K. S.; McCann, E.; Morozov, S.; Fal'ko, V. I.; Katsnelson, M.; Zeitler, U.; Jiang, D.; Schedin, F.; Geim, A. Unconventional quantum Hall effect and Berry's phase of  $2\pi$  in bilayer graphene. *Nat. Phys.* **2006**, *2*, 177–180.
- (44) Zhang, Y.; Tan, Y.-W.; Stormer, H. L.; Kim, P. Experimental observation of the quantum Hall effect and Berry's phase in graphene. *nature* **2005**, *438*, 201–204.
- (45) Feng, W.; Liu, C.-C.; Liu, G.-B.; Zhou, J.-J.; Yao, Y. First-principles investigations on the berry phase effect in spin-orbit coupling materials. *Comput. Mater. Sci.* **2016**, *112*, 428–447.
- (46) Wang, Z.; Jin, K.-H.; Liu, F. Quantum spin Hall phase in 2D trigonal lattice. *Nat. Commun.* **2016**, *7*, 12746.
- (47) Yan, B.; Felser, C. Topological materials: Weyl semimetals. *Annual Review of Condensed Matter Physics* **2017**, *8*, 337–354.
- (48) Hosur, P.; Qi, X. Recent developments in transport phenomena in Weyl semimetals. *Comptes Rendus. Physique* **2013**, *14*, 857–870.
- (49) Armitage, N.; Mele, E.; Vishwanath, A. Weyl and Dirac semimetals in three-dimensional solids. *Rev. Mod. Phys.* **2018**, *90*, No. 015001.
- (50) Wang, S.; Lin, B.-C.; Wang, A.-Q.; Yu, D.-P.; Liao, Z.-M. Quantum transport in Dirac and Weyl semimetals: a review. *Advances in Physics: X* **2017**, *2*, 518–544.
- (51) Crassee, I.; Sankar, R.; Lee, W.-L.; Akrap, A.; Orlita, M. 3D Dirac semimetal Cd 3 As 2: A review of material properties. *Physical Review Materials* **2018**, *2*, No. 120302.
- (52) Young, S. M.; Kane, C. L. Dirac semimetals in two dimensions. *Physical review letters* **2015**, *115*, No. 126803.
- (53) Fang, C.; Weng, H.; Dai, X.; Fang, Z. Topological nodal line semimetals. *Chinese Physics B* **2016**, *25*, 117106.
- (54) Burkov, A.; Hook, M.; Balents, L. Topological nodal semimetals. *Physical Review B—Condensed Matter and Materials Physics* **2011**, *84*, No. 235126.
- (55) Yang, M.-X.; Luo, W.; Chen, W. Quantum transport in topological nodal-line semimetals. *Adv. Phys.: X* **2022**, *7*, No. 2065216.
- (56) Fang, C.; Chen, Y.; Kee, H.-Y.; Fu, L. Topological nodal line semimetals with and without spin-orbital coupling. *Phys. Rev. B* **2015**, *92*, No. 081201.
- (57) Bader, R. F. W. Atoms in molecules. *Accounts of chemical research* **1985**, *18*, 9–15.
- (58) Bader, R. F. W. *Atoms in Molecules: A Quantum Theory*; Clarendon Press: Oxford, 1990.
- (59) Bader, R. F. W. A quantum theory of molecular structure and its applications. *Chem. Rev.* **1991**, *91*, 893–928.
- (60) Henkelman, G.; Arnaldsson, A.; Jónsson, H. A fast and robust algorithm for Bader decomposition of charge density. *Comput. Mater. Sci.* **2006**, *36*, 354–360.
- (61) Tang, W.; Sanville, E.; Henkelman, G. A grid-based Bader analysis algorithm without lattice bias. *J. Phys.: Condens. Matter* **2009**, *21*, No. 084204.
- (62) Yu, M.; Trinkle, D. R. Accurate and efficient algorithm for Bader charge integration. *J. Chem. Phys.* **2011**, *134*, No. 064111.
- (63) Gatti, C. Chemical bonding in crystals: new directions. *Zeitschrift f ü r Kristallographie - Crystalline Materials* **2005**, *220*, 399–457.
- (64) Espinosa, E.; Molins, E.; Lecomte, C. Hydrogen bond strengths revealed by topological analyses of experimentally observed electron densities. *Chem. Phys. Lett.* **1998**, *285*, 170–173.
- (65) Espinosa, E.; Alkorta, I.; Elguero, J.; Molins, E. From weak to strong interactions: A comprehensive analysis of the topological and energetic properties of the electron density distribution involving X–H ... F–Y systems. *J. Chem. Phys.* **2002**, *117*, 5529–5542.
- (66) Gatti, C.; Macchi, P. In *Modern Charge Density Analysis*; Gatti, C.; Macchi, P., Eds.; Springer: Dordrecht, Heidelberg, London, NY, 2012; pp 1–78.
- (67) Fradera, X.; Austen, M. A.; Bader, R. F. W. The Lewis Model & Beyond. *J. Phys. Chem. A* **1999**, *103*, 304–314.
- (68) Bochicchio, R.; Ponec, R.; Torre, A.; Lain, L. Titolo dell'articolo. *Theor. Chem. Acc.* **2001**, *105*, 292–298.
- (69) Baranov, A. I.; Kohout, M. Electron localization and delocalization indices for solids. *J. Comput. Chem.* **2011**, *32*, 2064–2076.
- (70) Golub, P.; Baranov, A. I. Domain overlap matrices from plane-wave-based methods of electronic structure calculation. *J. Chem. Phys.* **2016**, *145*, 154107.
- (71) Otero-de-la Roza, A.; Pendás, A. M.; Johnson, E. R. Quantitative electron delocalization in solids from maximally localized Wannier functions. *J. Chem. Theory Comput.* **2018**, *14*, 4699–4710.
- (72) Zhang, H.; et al. Topological Insulator in Bi<sub>2</sub>Se<sub>3</sub>: Observation of Surface State Quantum Hall Effect. *Science* **2009**, *325*, 178–181.
- (73) Chen, Y.; et al. Doping-Induced Inversion of Spin-Orbit Coupled Bands in Bi<sub>2</sub>Se<sub>3</sub>. *Phys. Rev. Lett.* **2009**, *103*, 166405.
- (74) Fu, L.; Kane, C. L. Topological Insulators with Inversion Symmetry. *Phys. Rev. B* **2007**, *76* (4), 045302.
- (75) Wang, G.; Zhu, X.-G.; Sun, Y.-Y.; Li, Y.-Y.; Zhang, T.; Wen, J.; Chen, X.; He, K.; Wang, L.-L.; Ma, X.-C.; Jia, J.-F.; Zhang, S. B.; Xue, Q.-K. Topological Insulator Thin Films of Bi<sub>2</sub>Te<sub>3</sub> with Controlled Electronic Structure. *Adv. Mater.* **2011**, *23* (26), 2929–2932.
- (76) Lv, B. Q.; Weng, H. M.; Fu, B. B.; Wang, X. P.; Miao, H.; Ma, J.; Richard, P.; Huang, X.-C.; Zhao, L. X.; Chen, G. F.; Fang, Z.; Dai, X.; Qian, T.; Ding, H. Experimental Discovery of Weyl Semimetal TaAs. *Phys. Rev. X* **2015**, *5* (3), 031013.
- (77) Xu, S.-Y.; Belopolski, I.; Alidoust, N.; Neupane, M.; Bian, G.; Zhang, C.; Sankar, R.; Chang, G.; Yuan, Z.; Lee, C.-C.; et al. Discovery of a Weyl Fermion Semimetal and Topological Fermi Arcs. *Science* **2015**, *349* (6248), 613–617.
- (78) Xu, Y.; et al. Weyl Semimetal Phase in WTe<sub>2</sub>. *Nat. Commun.* **2015**, *6*, 7795.
- (79) Ali, M. N.; Xiong, J.; Flynn, S.; Tao, J.; Gibson, Q. D.; Schoop, L. M.; Liang, T.; Haldolaarachchige, N.; Hirschberger, M.; Ong, N. P.; et al. Large Non-saturating Magnetoresistance in WTe<sub>2</sub>. *Nature* **2014**, *514* (7521), 205–208.
- (80) Taherinejad, M.; Garrity, K. F.; Vanderbilt, D. Wannier center sheets in topological insulators. *Phys. Rev. B* **2014**, *89* (11), No. 115102.
- (81) Tang, P.; Zhou, Q.; Zhang, S.-C. Multiple types of topological fermions in transition metal silicides. *Physical review letters* **2017**, *119*, No. 206402.
- (82) Butler, W. H.; Snyder, G. J. From Materials to Devices: An Introduction to Thermoelectrics. *Scr. Mater.* **2011**, *65*, 1089–1095.
- (83) Hébert, S.; Flahaut, D.; Martin, C.; Lemonnier, S.; Noudem, J.; Goupil, C.; Maignan, A.; Hejtmánek, J. Thermoelectric Properties of Perovskites: Sign Change of the Seebeck Coefficient and High Temperature Properties. *Prog. Solid State Chem.* **2007**, *35* (2), 457–467.
- (84) Rameshti, B. Z.; Asgari, R. Thermoelectric Effects in Topological Crystalline Insulators. *Phys. Rev. B* **2016**, *94* (20), 205401.
- (85) Shan, W.-Y.; Lu, H.-Z.; Xiao, D. Spin Hall Effect in Spin-Valley Coupled Monolayers of Transition Metal Dichalcogenides. *Phys. Rev. B* **2013**, *88* (12), 125301.
- (86) Bhowal, S.; Satpathy, S. Intrinsic Orbital and Spin Hall Effects in Monolayer Transition Metal Dichalcogenides. *Phys. Rev. B* **2020**, *102* (3), No. 035409.
- (87) Saitoh, E.; Ueda, M.; Miyajima, H.; Tatara, G. Conversion of spin current into charge current at room temperature: Inverse spin-Hall effect. *Appl. Phys. Lett.* **2006**, *88*, 182509.
- (88) Kimura, T.; Otani, Y.; Sato, T.; Takahashi, S.; Maekawa, S. Room-Temperature Reversible Conversion between Spin and Charge

- Currents Using the Spin Hall Effect. *Phys. Rev. Lett.* **2007**, *98*, No. 156601.
- (89) Ando, K.; Takahashi, S.; Harii, K.; Sasage, K.; Ieda, J.; Uchida, K.; Fujikawa, Y.; Matsuo, M.; Maekawa, S.; Saitoh, E. Electrical Detection of the Spin Hall Effect by the Inverse Spin Hall Effect. *Appl. Phys. Lett.* **2007**, *91*, 182503.
- (90) Giannozzi, P.; Baroni, S.; Bonini, N.; Calandra, M.; Car, R.; Cavazzoni, C.; Ceresoli, D.; Chiarotti, G. L.; Cococcioni, M.; Dabo, I.; Dal Corso, A.; de Gironcoli, S.; et al. QUANTUM ESPRESSO: A modular and open-source software project for quantum simulations of materials. *J. Phys.: Condens. Matter* **2009**, *21* (39), 395502.
- (91) Giannozzi, P.; et al. Advanced capabilities for materials modelling with Quantum ESPRESSO. *J. Phys.: Condens. Matter* **2017**, *29*, 465901.
- (92) Perdew, J. P.; Burke, K.; Ernzerhof, M. Generalized Gradient Approximation Made Simple. *Phys. Rev. Lett.* **1996**, *77*, 3865–3868.
- (93) Hamann, D. R. Optimized norm-conserving Vanderbilt pseudopotentials. *Phys. Rev. B* **2013**, *88*, No. 085117.
- (94) van Setten, M.; Giantomassi, M.; Bousquet, E.; Verstraete, M.; Hamann, D.; Gonze, X.; Rignanese, G.-M. The PseudoDojo: Training and grading a 85 element optimized norm-conserving pseudopotential table. *Comput. Phys. Commun.* **2018**, *226*, 39–54.
- (95) Tantardini, C.; Iliaš, M.; Giantomassi, M.; Kvashnin, A. G.; Pershina, V.; Gonze, X. Generating and grading 34 optimized norm-conserving Vanderbilt pseudopotentials for actinides and super-heavy elements in the PseudoDojo. *Comput. Phys. Commun.* **2024**, *295*, No. 109002.
- (96) Barma, M. Gaussian smearing of spin weight functions in models of phase transitions. *Journal of Physics A: Mathematical and General* **1983**, *16*, L745–L750.
- (97) Broyden, C. G. The Convergence of a Class of Double-Rank Minimization Algorithms 1. General Considerations. *IMA J. Appl. Math.* **1970**, *6* (1), 76–90.
- (98) Goldfarb, D. A Family of Variable-Metric Methods Derived by Variational Means. *Math. Comp.* **1970**, *24* (109), 23–26.
- (99) Shanno, D. F. Conditioning of Quasi-Newton Methods for Function Minimization. *Math. Comp.* **1970**, *24* (111), 647–656.
- (100) Steihaug, T. *Practical Methods of Optimization* Vol. 1: *Unconstrained Optimization*; Wiley: New York, 1980.
- (101) Cerasoli, F. T.; Supka, A. R.; Jayaraj, A.; Costa, M.; Siloi, I.; Ślawińska, J.; Curtarolo, S.; Fornari, M.; Ceresoli, D.; Buongiorno Nardelli, M. Advanced modeling of materials with PAOFLOW 2.0: New features and software design. *Comput. Mater. Sci.* **2021**, *200*, No. 110828.
- (102) Kawamura, M. FermiSurfer: Fermi-surface viewer providing multiple representation schemes. *Comput. Phys. Commun.* **2019**, *239*, 197–203.
- (103) Otero-de-la-Roza, A.; Blanco, M. A.; Pendás, A. M.; Luana, V. Critic: A new program for the topological analysis of solid-state electron densities. *Comput. Phys. Commun.* **2009**, *180*, 157–166.
- (104) Otero-de-la-Roza, A.; Johnson, E. R.; Luana, V. Critic2: A program for real-space analysis of quantum chemical interactions in solids. *Comput. Phys. Commun.* **2014**, *185*, 1007–10188.
- (105) Blum, V.; Gehrke, R.; Hanke, F.; Havu, P.; Havu, V.; Ren, X.; Reuter, K.; Scheffler, M. Ab initio molecular simulations with numeric atom-centered orbitals. *Comput. Phys. Commun.* **2009**, *180*, 2175–2196.
- (106) Havu, V.; Blum, V.; Havu, P.; Scheffler, M. Efficient O (N) integration for all-electron electronic structure calculation using numeric basis functions. *J. Comput. Phys.* **2009**, *228*, 8367–8379.
- (107) Lin, C.; Poncé, S.; Marzari, N. General invariance and equilibrium conditions for lattice dynamics in 1D, 2D, and 3D materials. *npj Comput. Mater.* **2022**, *8*, 236.
- (108) Gresch, D.; Autès, G.; Yazev, O. V.; Troyer, M.; Vanderbilt, D.; Bernevig, B. A.; Soluyanov, A. A. Z2Pack: Numerical implementation of hybrid Wannier centers for identifying topological materials. *Phys. Rev. B* **2017**, *95*, No. 075146.
- (109) Madsen, G. K.; Carrete, J.; Verstraete, M. J. BoltzTraP2, a program for interpolating band structures and calculating semi-classical transport coefficients. *Comput. Phys. Commun.* **2018**, *231*, 140–145.

CAS BIOFINDER DISCOVERY PLATFORM™

**ELIMINATE DATA SILOS. FIND WHAT YOU NEED, WHEN YOU NEED IT.**

A single platform for relevant, high-quality biological and toxicology research

Streamline your R&D

**CAS**   
A division of the  
American Chemical Society